Influence of Cu insertion on the thermoelectric properties of the quaternary cluster compounds Cu3M2Mo15Se19 (M = In, K) and Cu4In2Mo15Se19

Patrick Gougeon, Philippe Gall, Shantanu Misra, Adèle Léon, Christine Gendarme, Sylvie Migot, Jaafar Ghanbaja, Soufiane El Oualid, Bertrand Lenoir, Christophe Candolfi

Influence of Cu insertion on the thermoelectric properties of the quaternary cluster compounds $Cu_3M_2Mo_{15}Se_{19}$ (M = In, K) and $Cu_4In_2Mo_{15}Se_{19}$

Patrick Gougeon[1,*], Philippe Gall[1], Shantanu Misra[2], Adèle Léon[2], Christine Gendarme[2], Sylvie Migot[2], Jaafar Ghanbaja[2], Soufiane El Oualid[2], Bertrand Lenoir[2], Christophe Candolfi[2,*]

[1] *Sciences Chimiques de Rennes, UMR 6226 CNRS – Ecole Nationale Supérieure de Chimie de Rennes – Université de Rennes 1, Avenue du Général Leclerc, 35042 Rennes, France*

[2] *Institut Jean Lamour, UMR 7198 CNRS – Université de Lorraine, Campus ARTEM, 2 allée André Guinier, BP 50840, 54011 Nancy, France*

[*]Contact authors: patrick.gougeon@univ-rennes1.fr ; christophe.candolfi@univ-lorraine.fr

Abstract

Mo-based cluster compounds form a large class of materials with interesting thermoelectric properties primarily due to their very low lattice thermal conductivity. Here, we investigate the influence of the insertion of Cu on the crystal structures and thermoelectric properties of the ternaries $In_2Mo_{15}Se_{19}$ and $K_2Mo_{15}Se_{19}$. Inserting Cu^+ cations into the intercluster voids of the rhombohedral lattice enables adjusting the hole concentration, resulting in higher thermopower values with respect to the Cu-free compounds. While Cu^+ cations occupy a single crystallographic site in $Cu_3In_2Mo_{15}Se_{19}$ as in the Ag-containing analogues, a distinctive crystallographic feature of $Cu_3K_2Mo_{15}Se_{19}$ is the different distribution of these cations that reside on split positions. The high degree of structural disorder of these compounds gives rise

to very low lattice thermal conductivity κ_L, which directly depends on the total concentration of inserted cations. The sensitivity of the electronic and thermal properties to the Cu content is evidenced by a Cu-rich sample with nominal composition $Cu_4In_2Mo_{15}Se_{19}$ that exhibits enhanced power factor and reduced κ_L, yielding a peak *ZT* value of ~0.42 at 1145 K. The good thermoelectric performance and high melting point of these compounds make them potential candidates for thermoelectric applications above 1000 K.

1. Introduction

Thermoelectric materials have the remarkable ability to convert thermal gradients into an electrical current and vice versa, providing interesting avenues for powering or cooling electronic devices and harvesting waste heat released in the environment by various industrial processes.[1-4] Efficient thermoelectric energy conversion requires specific materials that simultaneously show high thermopower α, low electrical resistivity ρ and low lattice and electronic thermal conductivities κ_L and κ_e, respectively. All these electronic and thermal transport coefficients are embodied in the dimensionless thermoelectric figure of merit $ZT = \alpha^2 T/\rho(\kappa_L + \kappa_e)$, which is the fundamental quantity that governs the conversion efficiency at the operating absolute temperature T.[1-4] This mandatory, yet unusual combination of properties in a single compound poses a formidable challenge in the design of highly-efficient thermoelectric materials. Furthermore, because the conversion efficiency and output power of thermoelectric generators depends on the temperature difference across the thermoelectric compounds,[5-8] identifying novel materials with high *ZT* values and high melting points is also of particular interest. However, to date, only a handful of compounds are able to operate above 1000 K; a restricted list that includes the state-of-the-art Si-Ge alloys,[9,10] Zintl phases based on $Yb_{14}MnSb_{11}$ and $RE_{3-x}Te_4$ (*RE* = La, Nd, Pr, Gd),[11-17] and half-Heusler alloys.[18-20]

Due to their high melting points, typically as high as 2000 K, ternary and quaternary compounds based on molybdenum have emerged as an interesting class of possible thermoelectric materials for power generation applications.[21-34] The formation of aggregates between Mo and the pnictogens S, Se or Te, called clusters, is triggered by an average oxidation degree for Mo atoms of less than three. Thus far, a rich diversity of clusters formed by 3 up to 36 Mo atoms have been successfully synthesized yielding more than 40 different structural types.[35-38] The unit cell complexity, raising with the size of the clusters and the insertion of cations in the large intercluster voids, results in very low κ_L values on the order of 0.5 W m^{-1} K^{-1} above 300 K.[21-34] In addition to providing a route towards lowering the thermal transport, the insertion of these cations helps to approach charge balance determined by the number of electrons available for the formation of Mo-Mo bonds referred to as the metal electron count (MEC). Depending on the MEC value, either semiconducting or highly-doped semiconducting electronic properties can be obtained, allowing for a fine tuning of the power factor α^2/ρ.

Among the various above-mentioned aggregates, the series $M_{2n}(Mo_9X_{11})(Mo_{6n}X_{6n+2})$ (n = 1 to 4) contains mixtures of even- and odd-membered clusters that crystallize in the $R\bar{3}c$ space group. The first member of this homologous series $M_2(Mo_9X_{11})(Mo_6X_8)$, or equivalently $M_2Mo_{15}X_{19}$, can be obtained with a vast diversity of M atoms that includes M = K,[39] Rb [40] and Cs [41] for X = S and M = K,[42] Rb,[27] Ba [43] and Tl [42] for X = Se. Initially studied for their metallic and superconducting properties in the 1980's, the coexistence of charge density waves (CDW) and superconductivity has been recently demonstrated.[44] Previous theoretical calculations on the Mo_6X_8 and Mo_9X_{11} cluster units have indicated that the MEC can vary from 20 to 24 and from 32 to 36 electrons, respectively. Combining the optimal MEC of 24 and 36 for the Mo_6 and Mo_9 clusters, respectively, yields an optimum MEC of 60 for the $Mo_{15}X_{19}$ subnetwork,[33] expected to give rise to semiconducting properties. However, due to the monovalent nature of K, Rb, Cs, In and Tl, the total MEC of the $M_2Mo_{15}X_{19}$ compounds is equal to 54, explaining the

p-type metallic properties observed experimentally. Further optimization of their thermoelectric properties requires the insertion of additional cations such as Ag^+ or Cu^+ to bring the MEC closer to its optimum value. This strategy has been successfully applied for $In_2Mo_{15}Se_{19}$ and $Tl_2Mo_{15}Se_{19}$, for which the insertion of Ag^+ cations led to enhanced thermoelectric performance with peak *ZT* values of 0.45 and 0.20 at 1100 and 800 K for $Ag_3In_2Mo_{15}Se_{19}$ and $Ag_3Tl_2Mo_{15}Se_{19}$, respectively.[25,45]

Here, we extend this strategy to the ternaries $In_2Mo_{15}Se_{19}$ and $K_2Mo_{15}Se_{19}$ and demonstrate the successful insertion of Cu^+ cations, yielding the new quaternary compounds $Cu_3In_2Mo_{15}Se_{19}$ and $Cu_3K_2Mo_{15}Se_{19}$. What marks them as distinct from their Ag-bearing analogues is the different localization of the Cu^+ cations in the intercluster voids that show a strongly disordered character. Upon further adjusting the nominal Cu concentration to $Cu_4K_2Mo_{15}Se_{19}$, the thermoelectric performance was further improved, with a peak *ZT* of ~0.42 at 1145 K.

2. Experimental Section

2.1 Synthesis of polycrystalline samples and single-crystal growth

Cu, $K_2Mo_6Se_6$ or $In_2Mo_6Se_6$, $MoSe_2$ and Mo powders were used as starting reagents. $In_2Mo_6Se_6$ was obtained from a stoichiometric mixture of InSe, $MoSe_2$ and Mo heated at 1000°C in evacuated sealed silica tube for 36h. $MoSe_2$ was synthetized from the elements Se and Mo introduced in stoichiometric proportion into a silica tube sealed under a primary vacuum and subsequently heated at 800°C for 24h. $K_2Mo_6Se_6$ was obtained by cationic exchange according to the reaction $In_2Mo_6Se_6 + 2KCl \rightarrow K_2Mo_6Se_6 + 2InCl$. This reaction was carried out in a sealed silica tube under an applied temperature gradient between a hot side temperature of

800°C and a cold side temperature left at room temperature. InCl then condenses in the form of crystals of yellowish-reddish color at the cold side of the tube.

$Cu_3K_2Mo_{15}Se_{19}$ was synthesized from a well-homogenized stoichiometric mixture of the above-mentioned products. About five grams of the mixture was cold pressed into a cylinder and introduced into a Mo crucible that was further sealed with an arc-welded system. The crucible was heated at 1300°C for 48h in a graphite-resistor furnace working under a reduced argon pressure. Attempts at synthesizing $Cu_xK_2Mo_{15}Se_{19}$ compounds with $x \geq 3$ led to the formation of the Chevrel phase $Cu_xMo_6Se_8$ as a secondary phase, as previously observed for the quaternary compounds $Ag_3In_2Mo_{15}Se_{19}$ and $Ag_3Tl_2Mo_{15}Se_{19}$, for which $AgMo_6Se_8$ appears for Ag contents higher than $x = 3$.[25,45] Nevertheless, transport properties measurements performed on a sample of nominal composition $Cu_4K_2Mo_{15}Se_{19}$ evidenced distinct transport properties, suggesting slight differences in the actual Cu content between these two compounds (see below). This difference is likely due to the consolidation process that leads to a slight Cu deficiency, as already observed for several Ag-containing cluster compounds.[25,45] Small single crystals were obtained by prolonged annealing at 1400°C for 96h, a temperature at which the phase begins to decompose.

In contrast to $Cu_3K_2Mo_{15}Se_{19}$, the $Cu_xIn_2Mo_{15}Se_{19}$ compounds could not be obtained by direct syntheses from the initial products Cu, $In_2Mo_6Se_6$, $MoSe_2$ and Mo in the temperature range 900 – 1500°C, should it be in sealed silica tubes or Mo crucibles. These compounds could be only synthesized by heating mixed powders of Cu and $In_2Mo_{15}Se_{19}$ at 900°C in a sealed silica tube during 30h.

2.2 Structural determination of $Cu_3K_2Mo_{15}Se_{19}$ by single-crystal X-ray diffraction

A single crystal obtained at 1400°C was investigated on an Enraf-Nonius Kappa CCD goniometer (MoKα radiation, λ = 0.71073 Å). The absorption correction was applied using the analytical absorption software developed by de Meulenaer and Tompa. As a starting point, the crystal structure was solved by isomorphism with $K_2Mo_{15}Se_{19}$. All structure refinements and Fourier analyses were carried out using JANA2006.[46] After the refinement of the '$K_2Mo_{15}Se_{19}$' framework, a difference Fourier map showed significant electron densities at three different locations compatible with Cu sites. However, in contrast to the compounds $Ag_3In_2Mo_{15}Se_{19}$ (Ref. 25) and $Tl_2Mo_{15}S_{19}$ (Ref. 45) in which anharmonic effects were observed for the In or Tl atoms, only harmonic anisotropic displacement parameters were used for the K atoms. Refinement of the occupancy factor of the K position indicated full occupancy. On the other hand, a Cu deficiency was found for the single crystal investigated with a final stoichiometry corresponding to $Cu_{2.90(2)}K_2Mo_{15}Se_{19}$. Experimental data and X-ray structural refinement results are summarized in Table 1. The final fractional atomic coordinates and equivalent isotropic displacement parameters are given in Table 2, while the main interatomic bond lengths are gathered in Table 5. The supplementary crystallographic data for $Cu_{2.90(2)}K_2Mo_{15}Se_{19}$ can be obtained under the code CSD 2234547 at the Inorganic Crystal Structure Database.

2.3 Structural determination of $Cu_3In_2Mo_{15}Se_{19}$ by powder X-ray diffraction

Powder X-ray diffraction (PXRD) study was realized using a Bruker D8 Advance diffractometer (θ–2θ Bragg–Brentano geometry) equipped with a copper anode target to generate X-rays with a current of 40 mA and a voltage of 40 kV. A curved Ge(111) monochromator selecting the Cu-$Kα_1$ wavelength and a Lynx-Eye detector were used. The

measurement was performed from 8° to 130° with a step width of 0.008° and a counting time of 1.7 s per step. The PXRD pattern was refined using the JANA2006 software.[46] The peak shapes were modelled using Thompson-Cox-Hastings pseudo-Voigt functions. Berar's factors were applied to the estimated standard deviations to obtain more realistic values. Experimental data and X-ray structural refinement results are summarized in Table 3. The final fractional atomic coordinates and isotropic displacement parameters are given in Table 4, while the main interatomic bond lengths are gathered in Tables 5 and 6. The supplementary crystallographic data for $Cu_3In_2Mo_{15}Se_{19}$ can be obtained under the code CSD 2234549 at the Inorganic Crystal Structure Database.

2.4 Consolidation of the polycrystalline samples

Polycrystalline ingots of $Cu_xIn_2Mo_{15}Se_{19}$ (x = 3 or 4) and $Cu_3K_2Mo_{15}Se_{19}$ were finely ground into fine powders and densified by hot uniaxial pressing (HUP) under vacuum (about 10^{-2} mbar). The pressure was applied from the beginning of the temperature increase (8 K min^{-1}) to the end of the high-temperature dwell. Typical quantities of 5g of powders were introduced into a graphite die (Ø 12mm) previously coated with boron nitride. The applied load was 50 MPa at the beginning of the heating step and was gradually increased to 85 MPa when the sintering temperature (900°C for $Cu_xIn_2Mo_{15}Se_{19}$ and 1300°C for $Cu_3K_2Mo_{15}Se_{19}$) was reached. The dwell time was 2h for all experiments. The density of the pellets, determined from the weight and sample dimensions, was calculated to be around 95% of the theoretical density from crystallographic data.

2.5 Structural and chemical characterizations

Scanning electron microscopy (SEM) was carried out on small polished pieces of the polycrystalline samples using a Quanta FEG 650 (FEI) instrument in backscattering electron mode (BSE). The spatial distribution of the elements was assessed by electron dispersive X-ray spectroscopy (EDXS).

The chemical composition of the polycrystalline samples was determined by electron probe microanalyses (EPMA) using a JEOL JXA 8530F instrument. Polycrystalline $CuMo_6Se_8$ and $In_2Mo_{15}Se_{19}$ were used as standards to determine the concentration of Cu and In, while a polycrystalline sample of $K_2Mo_{15}Se_{19}$ was used for K, Mo and Se. In both cases, these samples were used to minimize the influence of absorption phenomena. The chemical formulas were obtained by normalizing the Mo content to 15 Mo atoms per chemical formula.

Transmission electron microscopy (TEM) analyses were conducted on thin slices prepared from the polycrystalline samples by the dual focused ion beam (FIB) – scanning electron microscope system using the in-situ lift-out technique. Scanning TEM (STEM) in high-angle annular dark-field (HAADF) and annular bright field (ABF) modes were performed with a JEOL ARM 200F – cold FEG TEM/STEM microscope operating at 200 keV and equipped with a spherical aberration (Cs) probe and image correctors.

2.6 Transport properties measurements

Measurements of the transport properties were performed on bar- and disc-shaped samples cut from the consolidated pellets using a diamond-wire saw. At low temperatures (5 – 300 K), the temperature dependence of the electrical resistivity, thermopower and thermal conductivity were measured simultaneously using the thermal transport option (TTO) of a Physical Property

Measurement System (PPMS, Quantum Design). Four copper bars were mounted on bar-shaped samples (typical dimensions of 8×2×2 mm^3) using a silver-containing conductive epoxy. Hall effect measurements were performed in the same temperature range and on the same sample using the ac transport option of the PPMS. The transverse electrical resistivity ρ_{xy} was measured under magnetic field $\mu_0 H$ ranging between – 1 and +1 T. Ohmic contacts were realized by attaching five copper wires onto the sample with a minute amount of conductive silver paste. Possible magnetoresistive contributions were dismissed by considering the antisymmetric part of ρ_{xy} under magnetic field reversal following the formula $\rho_H = \left[\rho_{xy}(+\mu_0 H) - \rho_{xy}(-\mu_0 H)\right]/2$. The Hall coefficient R_H was determined from the slope of the $\rho_H(\mu_0 H)$ curves in the limit $\mu_0 H \to 0$. The hole concentration p_H and mobilities μ_H were inferred from the single-band formulas $p_H = 1/R_H e$ and $\mu_H = R_H/\rho$ where e is the elementary charge.

Electrical resistivity and thermopower were measured at high temperatures (300 – 800 K) on a bar-shaped sample using a ZEM-3 apparatus (Ulvac-Riko). The thermal conductivity was determined in the same temperature range by measuring the thermal diffusivity a with a laser flash technique on a LFA 427 apparatus (Netzsch). Both quantities are interrelated via the specific heat C_p and density d according to the formula $\kappa = a C_p d$. As a first approximation, the Dulong-Petit value was used to estimate C_p in this temperature range while the temperature dependence of the density was neglected. For the Cu_4In_2 sample that exhibits the highest thermoelectric performance, these transport properties were measured up to 1145 K. The experimental uncertainty in the determination of the *ZT* values is estimated to be ~17%.[47]

3. Results and Discussion

3.1 Crystal structures

$Cu_3In_2Mo_{15}Se_{19}$, $Cu_4In_2Mo_{15}Se_{19}$ and $Cu_3K_2Mo_{15}Se_{19}$ are all Cu-filled variants of $In_2Mo_{15}Se_{19}$ and $K_2Mo_{15}Se_{19}$, which essentially differ from their Ag-containing analogues by the distribution of Cu^+ cations between the two cluster units $Mo_6Se_8Se_6$ and $Mo_9Se_{11}Se_6$. Their rhombohedral crystal structure, shown in Figure 1 along the [110] direction, is built up by the three-dimensional arrangement of these two clusters. Within the first unit $Mo_6Se_8Se_6$ (Figure 2), the Mo atoms form an octahedral cluster similar to that observed in Chevrel phases.[48,49] The Mo core in the second unit $Mo_9Se_{11}Se_6$ is a face-sharing bioctahedron (Figure 2). Their environments consist of 8 and 11 Se atoms, respectively, capping triangular faces with 6 additional ones in apical position. The three-dimensional Mo-Se framework can be viewed as resulting from the substitution of the 6 apical Se atoms of the $Mo_6Se_8Se_6$ (respectively $Mo_9Se_{11}Se_6$) units by the 6 inner Se atoms of the six adjacent $Mo_9Se_{11}Se_6$ (respectively $Mo_6Se_8Se_6$) units of their nearest environment.

Monovalent (K^+, Rb^+, Cs^+, In^+ or Tl^+) or divalent (Ba^{2+}) cations can occupy the large empty cavities formed by 11 chalcogen atoms, resulting in an Edshammar 11-polyhedron (denoted hereafter as ^{11}E) (Figures 3 and 4).[50,51] In the quaternary compounds $Ag_3In_2Mo_{15}Se_{19}$,[25] $Ag_3Tl_2Mo_{15}Se_{19}$[45] and $Ag_3K_2Mo_{15}Se_{19}$,[32] Ag^+ cations occupy the small, highly-distorted triangular bipyramidal voids located between adjacent ^{11}E polyhedra along the three directions $[841]$, $[\bar{4}41]$ and $[\bar{4}\bar{8}1]$ (see Figure 3). The presence of Ag^+ results in a modification of their atomic environment, evidenced by a clear shift of the later atoms towards the Se5 atoms while they move away from the Se3 and Se4 atoms.

The Cu^+ cations in $Cu_3In_2Mo_{15}Se_{19}$ are distributed similarly to Ag^+ in $Ag_3In_2Mo_{15}Se_{19}$ and thus only occupy the site 1 in Figure 3. Consequently, the Cu atoms occupy distorted triangular bipyramid sites located between two consecutive In sites. Nevertheless, because of the proximity of the copper sites that are delocalized on either side of the triangular base and only distant of 1 Å, the Cu atoms are in pseudo-tetrahedral sites of Se atoms with Cu-Se distances ranging from 2.514(19) Å to 2.828(14) Å (Figure 4). In $Cu_3K_2Mo_{15}Se_{19}$, a different arrangement is observed for the Cu^+ cations which occupy both the distorted triangular bipyramidal (site 1 in Figure 3) and octahedral sites (site 2 in Figure 3) located between adjacent Edshammar polyhedra (see Figure 3). In the site 2, the Cu^+ cations are distributed over four crystallographic positions linked two by two by the inversion center corresponding to a 18*d* Wyckoff position and also to the center of the octahedron. Consequently, both Cu1 and Cu2 are surrounded by four Se atoms forming distorted tetrahedra. The Cu1 and Cu2 sites are partially occupied (19 and 17%, respectively) leading to an overall occupancy of 72% of the octahedral site. The Cu-Se distances range between 2.499(6) Å and 2.557(6) Å and between 2.213(6) Å and 2.523(6) Å for the Cu1 and Cu2 sites, respectively. Likewise, the Cu3 atoms partially occupy (15%) the center of the distorted triangular bipyramids and thus, are in triangular coordination with Cu3-Se distances of 2.510(5) Å and one Cu3-Se3 distance of 2.520(5) Å. The other two Se4 atoms constituting the apices of the bipyramids are at 3.379(7) Å. Interestingly, while the insertion of Ag modifies the environment of K^+ in $Ag_3K_2Mo_{15}Se_{19}$,[32] this influence is no longer observed in the Cu compounds, with the K^+ environment (Figure 5) being similar to that observed in $K_2Mo_{15}Se_{19}$.[42,44] The bond valence sum (BVS) calculations lead to values of +1.13, +1.07 and +0.61 for the Cu1, Cu2, and Cu3 atoms, respectively.[52] The lower value for the Cu3 atom is due to its small occupancy factor. From an electronic point of view, the increase in the total cationic charge due to the insertion of Ag and Cu leads to a reduction of the clusters with an average Mo oxidation state of +2.4 (that is, 54 electrons distributed over the Mo_6 and Mo_9 clusters) in the

ternary $M_2Mo_{15}Se_{19}$ phases (M = In, K) and +2.2 (that is, 57 electrons distributed over the Mo_6 and Mo_9 clusters) in $Cu_3In_2Mo_{15}Se_{19}$ and $Cu_3K_2Mo_{15}Se_{19}$ (+2.21 in the single crystal investigated). These differences point to an evolution of the Mo-Mo distances in both clusters, which is confirmed by variations in the Mo-Mo distances observed between $K_2Mo_{15}Se_{19}$ and $Cu_3K_2Mo_{15}Se_{19}$ (or equivalently between $In_2Mo_{15}Se_{19}$ and $Cu_3In_2Mo_{15}Se_{19}$). These characteristics are in agreement with those predicted by the COHP curves calculated on the host structures $M_2Mo_{15}Se_{19}$.[33] The COHP curves for the Mo-Mo bonds in the Mo_6 and Mo_9 clusters show that the vacant bands at the top of the valence band manifold have mostly a weakly-bonding or weakly anti-bonding character. Thus, the observed shortening of the intratriangle Mo2-Mo2, intertriangle Mo1-Mo1 and Mo2-Mo3 distances (Figure 6) is consistent with the Mo-Mo bonding character that binds electronic bands above the Fermi level in the $M_2Mo_{15}Se_{19}$ phases (M = In, K).[33] In contrast, the anti-bonding character of the intra-triangular Mo3-Mo3 bond explains the increase in this distance observed in the Ag and Cu compounds.

A key structural feature of these compounds is the smeared electronic density characterizing the inserted cations that requires introducing two distinct crystallographic sites. Both the large anisotropic thermal displacement parameters and the presence of several local minima evidence a strong static disorder of the cation sites. The resulting distribution of Cu^+ cations in $Cu_3K_2Mo_{15}Se_{19}$ differs from that observed previously for the Ag-containing compounds $Ag_3In_2Mo_{15}Se_{19}$,[25] $Ag_3Tl_2Mo_{15}Se_{19}$[31] and $Ag_3K_2Mo_{15}Se_{19}$[32]. The strongly disordered character of the cations in the intercluster voids is a universal property of Mo cluster compounds, which has been equally observed in various thermoelectric compounds such as clathrates, tetrahedrites, Zn_4Sb_3, VAl_{10} or InTe,[53-69] all of them showing extremely low lattice thermal conductivity due to the associated low-energy optical phonon modes that efficiently disrupt the acoustic dispersions.

3.2 Crystal structure, phase purity and chemical composition of the polycrystalline samples

The room-temperature powder X-ray diffraction patterns of $Cu_3In_2Mo_{15}Se_{19}$, $Cu_4In_2Mo_{15}Se_{19}$ and $Cu_3K_2Mo_{15}Se_{19}$ (Figures S1 to S3 in ESI) confirm that all of them crystallize with the hexagonal rhombohedral unit cell (space group $R\bar{3}c$), consistent with refinements of the single-crystal X-ray diffraction data. While a small amount of the Chevrel phase $Cu_xMo_6Se_8$ is present in the $Cu_4In_2Mo_{15}Se_{19}$ sample due to the Cu-rich nominal composition, both $Cu_3In_2Mo_{15}Se_{19}$ and $Cu_3K_2Mo_{15}Se_{19}$ were found to be phase pure within the detection limits of PXRD.

The phase homogeneity and spatial distribution of the elements were further probed by scanning electron microscopy (SEM). The backscattered electron images and corresponding elemental maps (Figures S4 to S6 in ESI) confirm an overall good chemical homogeneity of the polycrystalline samples. In addition to very small amounts of molybdenum oxides observed in all samples, these analyses evidence spatial fluctuations of Cu and K at the microscale in the Cu_3K_2 sample, with the presence of Cu-rich regions that correspond to K-poor regions. This observation also characterizes the Cu_4In_2 sample while the spatial distribution of Cu and In appears more homogeneous in the Cu_3In_2 sample. The presence of these fluctuations in the cationic distribution suggests that some deviations between the nominal and actual compositions exist, which is confirmed by wavelength dispersive X-ray spectroscopy (WDXS). The actual compositions, determined to be $Cu_{2.75}In_{2.05}Mo_{15}Se_{18.3}$, $Cu_{3.4}In_{1.8}Mo_{15}Se_{18.4}$ and $Cu_{1.18}K_{1.86}Mo_{15}Se_{18.6}$, indicate deviations in the overall cation content mainly due to an under-stoichiometry in Cu. This Cu deficiency in the matrix is likely due to the diffusion of Cu out of the intercluster voids due to the high temperatures required for the sintering process. The tendency of under-stoichiometry in the total cation content is also observed in single-crystalline specimens grown by recrystallization at temperatures on the order of 1700 K. Note that refinements of the single-crystalline X-ray diffraction data have not indicated the presence of

Se vacancies, indicative of the good thermal stability of the cluster skeleton. This cationic under-stoichiometry can be nevertheless partially counterbalanced by starting from a Cu-rich nominal composition, as shown by the higher Cu content measured in the $Cu_4In_2Mo_{15}Se_{19}$ sample with respect to $Cu_3In_2Mo_{15}Se_{19}$. Because the cation concentration governs the MEC, differences in the actual chemical compositions are expected to impact the thermoelectric properties, which is experimentally confirmed by the transport data discussed below.

Further analyses of the crystal structure of polycrystalline $Cu_3K_2Mo_{15}Se_{19}$ and $Cu_4In_2Mo_{15}Se_{19}$ were carried out using scanning transmission electron microscopy (STEM). Figure 7 shows selected-area electron diffraction (SAED) patterns of $Cu_3K_2Mo_{15}Se_{19}$ (Figure 7a) and $Cu_4In_2Mo_{15}Se_{19}$ (Figure 7d) taken along the [010] and [001] zone axis, respectively. Both patterns match well with the refined crystal structures and do not show the presence of extra reflections that would be indicative of a lattice modulation. Furthermore, no streaks, indicative of short-range ordering, are observed in these patterns. The high-angle annular dark-field (HAADF) and annular bright-field (ABF) images (Figures 7b, 7c, 7e and 7f) enable a direct visualization of the atomic columns characterizing these crystal structures. Because the contrast in the HAADF images scales with the atomic number Z roughly as Z^n (with $1 < n < 2$), only the Mo and Se atoms are visible for $Cu_3K_2Mo_{15}Se_{19}$ while In, Mo and Se are observed for $Cu_4In_2Mo_{15}Se_{19}$. The positions of the lighter cations Cu^+ and K^+ can be identified in the ABF images for which the contrast is based on wave interference. The displays of each element are shown in the magnified images, overlaid with the relevant fragments of the structural model.

For $Cu_3K_2Mo_{15}Se_{19}$, the zig-zag-like chains of Mo-Se clusters running in the *ac* plane are visible (Figures 7b and 7c). In this layered-like arrangement, the K^+ cations are located in the voids between two consecutive chains. The Cu^+ cations are observed between two consecutive K-Se chains in the ABF images. The presence of bright and darker atomic columns is consistent with the partial occupation of Cu on its crystallographic site. The EDS elemental maps (Figure

S7 in the ESI file) show an overall good chemical homogeneity at this scale, with the presence of areas where slight spatial fluctuations in the Cu content can nevertheless be observed.

The HAADF and ABF images (Figures 7e and 7f) of $Cu_4In_2Mo_{15}Se_{19}$ taken along the [001] zone axis show the Mo and Se sublattices, centered by the heavy In^+ cations and forming a double flower-like structure with a hexagonal symmetry consistent with structural refinements. The lighter Cu^+ cations are visible in the ABF images forming a ring-like arrangement and located between consecutive Se columns. Intensity profiles taken at various locations (not shown) are consistent with a random, partial distribution of the Cu^+ cations on their crystallographic sites, confirming the absence of short-range ordering. Similar to $Cu_3K_2Mo_{15}Se_{19}$, spatial fluctuations in the Cu content can be observed in some specific areas in the EDS elemental maps (Figure S8 in the ESI file) as well as In-rich and Mo-rich precipitates. Except for these regions, the spatial distribution of the four elements appears relatively homogeneous at this scale.

3.3 Transport properties

The temperature dependences of the electrical resistivity ρ and thermopower α of the three compounds are shown in Figures 8a and 8b, respectively. In contrast to the semiconducting behavior observed for the Cu_4In_2 sample, the $\rho(T)$ curves characterizing the Cu_3K_2 and Cu_3In_2 compounds show a more complex behavior. For Cu_3In_2, $\rho(T)$ initially decrease from 5 K up to about 100 K where an upturn in $\rho(T)$ occurs. Above this temperature, the ρ values slightly increase upon warming to about 350 K before decreasing again monotonically up to 800 K. The difference in $\rho(T)$ between both samples trends with the increase in the nominal Cu content, suggesting variations in the carrier concentration and mobility due to differing actual Cu concentrations.

For Cu_3K_2, $\rho(T)$ is characterized by a bell-shape behavior with a maximum reached near 150 K. Above 300 K, the ρ values smoothly decrease with increasing temperature to 800 K. The low-temperature behavior is reminiscent to that observed in the Cu-free compound $K_2Mo_{15}Se_{19}$, shown to originate from a CDW order that sets in below 200 K.[44] However, the onset of this transition leaves clear signatures on all the transport coefficient with, in particular, a concomitant increase in the α values due to the partial removal of electronic states near the Fermi level. In the present case, a survival of the CDW state upon inserting Cu can be ruled out due to the absence of similar fingerprint in $\alpha(T)$ (see Figure 8b). Thus, this behavior may be ascribed to the multiband nature of transport that characterizes the $M_2Mo_{15}Se_{19}$ compounds.[23,28,33]

This last conclusion is supported by the temperature dependence of $\alpha(T)$, which shows a conventional linear dependence above 300 K for all samples, reaching 68 and 87 μV K^{-1} at 800 K for the Cu_3K_2 and Cu_4In_2 compounds, respectively. The α values trend with the MEC set by the total cation concentration determined by EPMA analyses, with an increase in α from Cu_3K_2 ($n_{cation}^{EPMA} = 3.04$) to Cu_4In_2 ($n_{cation}^{EPMA} = 5.2$) through Cu_3In_2 ($n_{cation}^{EPMA} = 4.8$). In contrast, non-linear dependences emerge below 300 K. Both the Cu_3In_2 and Cu_4In_2 samples exhibit a faster decrease upon cooling below 100 K. Unlike these two compounds, the Cu_3K_2 sample shows a weaker upturn slightly below 300 K followed by a linear decrease upon further cooling to 50 K. This temperature marks a transition from positive to negative α values, with the negative sign persisting down to 5 K. This surprising finding, only observed so far in the cluster compound $Cs_2Mo_{12}Se_{14}$,[26] indicates a crossover from a dominant hole-like response above 50 K to an electron-like signal prevailing at lower temperatures. These results support a multiband character of the transport usually observed in this family of compounds,[21-34] with the α values resulting from a balance between hole-like and electron-like contributions.

The *p*-type nature of the transport prevailing in these compounds is confirmed by low-temperature Hall effect measurements (Figure S9 in the ESI). For all samples, the Hall coefficient R_H remains positive in the entire temperature range, in agreement with the sign of α above 50 K. For Cu_3K_2, the opposite signs of R_H and α below 50 K further confirms the multiband nature of transport. At 300 K, the hole concentration p_H, derived from a single-carrier model, is on the order of ~10^{22} cm^{-3} in Cu_3K_2, in agreement with its metallic nature. p_H decreases to 5.2×10^{21} cm^{-3} and 4.1×10^{21} cm^{-3} at 300 K in the Cu_3In_2 and Cu_4In_2 compounds, respectively. The lower p_H values inferred for Cu_4In_2 with respect to Cu_3In_2 is in line with the increased MEC in the former due to the higher actual Cu content. In both samples, p_H tends to decrease upon cooling to 5 K (Figure S10 in the ESI). These dependences depart from the expected nearly temperature-independent behavior of degenerate semiconductors with one dominant carrier type, further supporting multiband transport. For all samples, the Hall mobility μ_H is extremely low, amounting to only around 1 cm^2 V^{-1} s^{-1} without strong temperature variations over the entire temperature range. These low mobility values can be primarily attributed to the strongly disordered character of the Cu^+ cations residing in the intercluster voids, as observed in other tunnel-like compounds such as InTe or $Tl_{0.6}Mo_3S_5$ for instance.[69-73]

The total thermal conductivity κ of the three compounds as a function of temperature is shown in Figure 9a. Common to all compounds based on $Mo_{15}X_{19}$ clusters is the behavior of $\kappa(T)$, which mirrors that observed in glass-like compounds with the absence of a well-defined Umklapp peak at low temperatures and very low κ values. For all compounds, $\kappa(T)$ increases with increasing temperature nearly linearly from 200 up to 800 K, reaching a maximum value of 1.5 W m^{-1} K^{-1}. While $\kappa(T)$ is similar for the three compounds above 300 K, some differences can be observed below 200 K with notably the κ values of the In compounds being significantly lower compared to the K compound. The electronic thermal conductivity κ_e was calculated using the Wiedemann-Franz law $\kappa_e = LT/\rho$ where L is the Lorenz number, the temperature

dependence of which has been estimated as a first approximation using a single-parabolic band model. Replacing In for K results in a significant reduction in the lattice thermal conductivity $\kappa_L(T) = \kappa(T) - \kappa_e(T)$ (Figure 9b), which shows a twofold decrease at 800 K from 1.05 W m^{-1} K^{-1} in Cu_3K_2 to 0.75 W m^{-1} K^{-1} in Cu_3In_2. Particularly noteworthy is the strong sensitivity of κ_L to the total cation content, with a further 25% decrease in κ_L to 0.55 W m^{-1} K^{-1} at 800 K in the Cu_4In_2 sample with respect to Cu_3In_2. This lowering can be attributed to the additional Cu^+ cations inserted in the former that contribute to enhance the disorder in the unit cell. The higher κ_L values of the Cu_3K_2 compound compared to the In compounds is primarily due to the lower cation content that outweighs the more disordered character of Cu in Cu_3K_2.

The lowest κ_L value achieved in the Cu_4In_2 compound, similar to those achieved in the Zintl phases $Yb_{14}MnSb_{11}$ and $RE_{3-x}Te_4$ (R = La, Nd, Pr, Gd),[11-17] is very close to the minimum lattice thermal conductivity κ_{min} of 0.35 W m^{-1} K^{-1}, calculated from the measured sound velocities according to the model of Cahill and Pohl.[74] The fact that κ_L nears κ_{min} suggests that the thermal transport has reached its minimum value, which, within the model considered, occurs when the phonon mean free path is on the order of the mean interatomic distance of the crystal structure. Several key ingredients concur to the minimization of κ_L naturally realized in most of Mo-based cluster compounds. A first general aspect is the large number of atoms per unit cell that leads to a high number of low-velocity optical modes that contribute weakly to heat transport and enhance Umklapp scattering events. The presence of strongly disordered cations in the intercluster voids provides a second important ingredient that strongly limit κ_L. This disorder, modelled by large, anisotropic thermal displacement parameters, leads to low-energy optical modes that limit the phase space over which the acoustic branches disperse. This characteristic, shared by several cage-like or tunnel-like compounds,[53-69,73] has been evidenced by inelastic neutron scattering in the quasi-1D cluster compounds AMo_6Se_6 (A = K, Rb, Cs, In and Tl) for which, the dynamics of the cations shapes the low-energy region of the phonon

spectrum.[75] In addition, the likely complex potential landscape of the Cu, K and In cations results in broadened distributions of the low-energy optical modes that further contribute to promote three-phonon scattering processes involving the acoustic modes. This beneficial role of inserting cations is qualitatively equivalent to that recently evidenced in Mg_3Sb_2 where the introduction of interstitial Cu advantageously modifies the phonon density of states and drives a significant increase in three-phonon scattering rate.[76] The induced broadening is expected to lower the structure factor of low-energy optical modes, possibly leading to difficulties in experimentally resolving them by neutron spectroscopy, as recently evidenced in InTe for instance.[69] Nevertheless, high-resolution neutron and/or synchrotron measurements would be worthwhile in clarifying the role played by the nature and crystallographic position of the cations on the lattice dynamics of these compounds.

The dimensionless thermoelectric figure of merits *ZT*, shown in Figure 10 as a function of temperature, are comparable to those achieved previously for the Ag-containing quaternary compounds with moderate peak values of 0.10 and 0.15 achieved at 800 K for the Cu_3K_2 and Cu_3In_2 compounds, respectively. The peak *ZT* of 0.25 achieved at 800 K in the Cu_4In_2 compound is further enhanced to ~0.42 at 1145 K due to its lower electrical resistivity and thermal conductivity. At this temperature, the *ZT* values tend to level off due to the thermal activation of minority carriers that decrease the thermopower values. This maximum *ZT* is similar to that obtained in the $Ag_3In_2Mo_{15}Se_{19}$ compound (~0.45 at 1100 K),[25] which is the highest *ZT* value obtained so far in this family of compounds. Relative to the previously studied Ag-containing compounds, the distinct crystallographic positions of the Cu atoms have little influence on the overall thermoelectric performance. Rather, these results highlight the need for further decreasing the hole concentration by possibly inserting divalent or trivalent cations into the intercluster voids.

4. Conclusion

We reported on the synthesis, crystal structure and transport properties over a wide range of temperatures of the novel quaternary Mo-based cluster compounds $Cu_3M_2Mo_{15}Se_{19}$ with M = K and In. The distinct distribution of the Cu atoms in the intercluster voids in these two compounds is the main crystallographic characteristic that distinguishes them from their Ag-containing analogues. All the three samples behave as degenerate semiconductors with relatively low electrical resistivity and moderate thermopower values. These measurements further highlight the sensitivity of the electronic properties to the Cu concentration. Counterbalancing the slight loss of Cu by starting from the nominal composition $Cu_4In_2Mo_{15}Se_{19}$ led to an enhanced power factor compared to that achieved in the $Cu_3In_2Mo_{15}Se_{19}$ sample. However, the multiband character of the electronic transport limits the thermopower values at high temperatures compared to the higher values achieved in the best-performing *p*-type compounds above 1000 K. Common to all Mo-based cluster compounds studied so far, the lattice thermal conductivity is close to be minimal, due to the strong local disorder of the Cu atoms. This property is the key ingredient that leads to a peak ZT of ~0.42 at 1145 K for $Cu_4In_2Mo_{15}Se_{19}$. This value, comparable to that achieved in the isomorphous compound $Ag_3In_2Mo_{15}Se_{19}$, shows that the intrinsically poor thermal transport and high melting point of these compounds make them interesting candidates for thermoelectric applications operating above 1000 K. Further decreasing the hole concentration through insertion of aliovalent elements may provide a route to achieving higher thermoelectric performance.

Conflicts of interest

There are no conflicts to declare.

References

1 D. M. Rowe, *Thermoelectrics Handbook: Macro to Nano*, CRC Press, Boca Raton, FL, 2006.

2 H. J. Goldsmid, *Thermoelectric Refrigeration*, Springer, New York, USA, 1964.

3 R. Freer, D. Ekren, T. Ghosh, K. Biswas, P. Qiu, S. Wan, L. Chen, S. Han, C. Fu, T. Zhu, A. K. M. Ashiquzzaman Shawon, A. Zevalkink, K. Imasato, G. J. Snyder, M. Ozen, K. Saglik, U. Aydemir, R. Cardoso-Gil, E. Svanidze, R. Funahashi, A. V. Powell, S. Mukherjee, S. Tippireddy, P. Vaqueiro, F. Gascoin, T. Kyratsi, P. Sauerschnig and T. Mori, *J. Phys.: Energy*, 2022, **4**, 022002.

4 T. Hendricks, T. Caillat and T. Mori, *Energies*, 2022, **15**, 7307.

5 D. M. Rowe, in *Thermoelectrics and its Energy Harvesting: Modules, Systems, and Applications in Thermoelectrics* (Ed: D. M. Rowe), CRC Press, Boca Raton, FL, 2012.

6 N. Jaziri, A. Boughamoura, J. Müller, B. Mezghani, F. Tounsi and M. Ismail, *Energy Rep*. 2019, **6**, 264.

7 R. He, G. Schierning and K. Nielsch, *Adv. Mater. Technol.*, 2018, **3**, 1700256.

8 F. Freer and A. V. Powell, *J. Mater. Chem. C*, 2020, **8**, 441.

9 J. Yang and T. Caillat, *MRS Bull.*, 2006, **31**, 224–229.

10 C. B. Vinning and J.-P. Fleurial, in *Silicon-Germanium: An Overview of Recent Development* (AIP Press), pp. 87–120, 1993.

11 S. R. Brown, S. M. Kauzlarich, F. Gascoin and G. J. Snyder, *Chem. Mater.*, 2006, **18**, 1873–1877.

12 J. H. Grebenkemper, Y. Hu, D. Barrett, P. Cogna, C.-K. Huang, S. K. Bux and S. M. Kauzlarich, *Chem. Mater.*, 2015, **27**, 5791–5798.

13 C. J. Perez, G. Cerretti, E. L. K. Wille, K. P. Devlin, N. S. Grewal, A. P. Justl, M. Wood, S. K. Bux and S. M. Kauzlarich, *Chem. Mater.*, 2021, **33**, 8059–8069.

14 A. F. May, J.-P. Fleurial and G. J. Snyder, *Phys. Rev. B*, 2008, **78**, 125205.

15 D. Cheikh, B. E. Hogan, T. Vo, P. V. Allmen, K. Lee, D. M. Smiadak, A. Zevalkink, B. S. Dunn, J.-P. Fleurial and S. K. Bux, *Joule*, 2018, **2**, 698–709.

16 S. J. Gomez, D. Cheikh, T. Vo, P. V. Allmen, K. Lee, M. Wood, G. J. Snyder, B. S. Dunn, J.-P. Fleurial and S. K. Bux, *Chem. Mater.*, 2019, **31**, 4460–4468.

17 F. Qin, S. A. Nikolaev, A. Suwardi, M. Wood, Y. Zhu, X. Tan, U. Aydemir, Y. Ren, Q. Yan, L. Hu and G. J. Snyder, *Chem. Mater.*, 2020, **32**, 10130–10139.

18 Y. Liu, C. Fu, K. Xia, J. Yu, X. Zhao, H. Pan, C. Felser and T. Zhu, *Adv. Mater.*, 2018, **30**, 1800881.

19 X. Yan, W. Liu, H. Wang, S. Chen, J. Shiomi, K. Esfarjani, H. Wang, D. Wang, G. Chen and Z. Ren, *Energy Environ. Sci.* 2012, **5**, 7543–7548.

20 L. Huang, Q. Zhang, B. Yuan, X. Lai, X. Yan, Z. Ren, *Mater. Res. Bull.* 2016, **76**, 107– 112.

21 C. Candolfi, P. Gougeon, P. Gall, M. Potel, A. Dauscher and B. Lenoir, in *Thermoelectric Properties of Ternary and Quaternary Mo6 and Mo9 Cluster Selenides.* Jean-François Halet (ed), *Ligated Transition Metal Clusters in Solid-state Chemistry*, 180, Springer, pp.125–141, **2019**.

22 T. Zhou, B. Lenoir, M. Colin, A. Dauscher, R. Al Rahal Al Orabi, P. Gougeon, M. Potel and E. Guilmeau, *Appl. Phys. Lett.*, 2011, **98**, 162106.

23 T. Zhou, M. Colin, C. Candolfi, C. Boulanger, A. Dauscher, E. Santava, J. Hejtmanek, P. Baranek, R. Al Rahal Al Orabi, M. Potel, B. Fontaine, P. Gougeon, R. Gautier and B. Lenoir, *Chem. Mater.*, 2014, **26**, 4765−4775.

24 R. Al Rahal Al Orabi, P. Gougeon, P. Gall, B. Fontaine, R. Gautier, M. Colin, C. Candolfi, A. Dauscher, J. Hejtmanek, B. Malaman and B. Lenoir, *Inorg. Chem.*, 2014, **53**, 11699−11709.

25 P. Gougeon, P. Gall, R. Al Rahal Al Orabi, B. Fontaine, R. Gautier, M. Potel, T. Zhou, B. Lenoir, M. Colin, C. Candolfi and A. Dauscher, *Chem. Mater.*, 2012, **24**, 2899−2908.

26 R. Al Rahal Al Orabi, B. Fontaine, R. Gautier, P. Gougeon, P. Gall, Y. Bouyrie, A. Dauscher, C. Candolfi and B. Lenoir, *Inorg. Chem.*, 2016, **55**, 6616−6624.

27 G. Daigre, P. Gougeon, P. Gall, R. Gautier, O. Guillou, J.-B. Vaney, C. Candolfi, A. Dauscher and B. Lenoir, *J. Solid State Chem.*, 2016, **237**, 1−6.

28 P. Masschelein, C. Candolfi, A. Dauscher, C. Gendarme, R. Al Rahal Al Orabi, P. Gougeon, M. Potel, P. Gall, R. Gautier and B. Lenoir, *J. Alloys Compd.*, 2018, **739**, 360−367.

29 M. Colin, T. Zhou, B. Lenoir, A. Dauscher, R. Al Rahal Al Orabi, P. Gougeon, M. Potel, P. Baranek and C. Semprimoschnig, *J. Electron. Mater.*, 2012, **41**, 1360−1364.

30 P. Gougeon, P. Gall, O. Merdrignac-Conanec, L. Aranda, A. Dauscher, C. Candolfi and B. Lenoir, *Inorg. Chem.*, 2017, **56**, 9684−9692.

31 P. Gougeon, P. Gall, R. Al Rahal Al Orabi, B. Boucher, B. Fontaine, R. Gautier, A. Dauscher, C. Candolfi and B. Lenoir, *Inorg. Chem.*, 2019, **58**, 5533−5542.

32 G. Daigre, P. Gougeon, P. Gall, O. Merdrignac-Conanec, R. Al Rahal Al Orabi, R. Gautier, A. Dauscher, C. Candolfi and B. Lenoir, *ACS Appl. Energy Mater.*, 2020, **3**, 2846–2855.

33 R. Al Rahal Al Orabi, B. Boucher, B. Fontaine, P. Gall, C. Candolfi, B. Lenoir, P. Gougeon, J.-F. Halet and R. Gautier, *J. Mater. Chem. C*, 2017, **5**, 12097–12104.

34 S. M. Butorin, K. O. Kvashnina, M. Klintenberg, M. Kavcic, M. Zitnik, K. Bucar, P. Gougeon, P. Gall, C. Candolfi and B. Lenoir, *ACS Appl. Energy Mater.*, 2018, **1**, 4032–4039.

35 P. Gougeon, M. Potel, J. Padiou and M. Sergent, *Mater. Res. Bull.*, 1988, **23**, 453−460.

36 S. Picard, P. Gougeon and M. Potel, *Acta Crystallogr.*, 1997, **C53**, 1519−1521.

37 S. Picard, P. Gougeon and M. Potel, *Angew. Chem., Int. Ed.*, 1999, **38**, 2034−2036.

38 S. Picard, P. Gougeon and M. Potel, *Acta Crystallogr., Sect. C: Cryst. Struct. Commun.*, 2001, **57**, 663−664.

39 S. Picard, P. Gougeon and M. Potel, *Acta Cryst.*, 2002, **E58**, i12.

40 S. Picard, J.-Y. Saillard, P. Gougeon, H. Noel and M. Potel, *J. Solid State Chem.*, 2000, **155**,

417.

41 P. Gougeon, M. Potel and M. Sergent, *Acta Cryst.*, 1989, **C45**, 1285.

42 R. Chevrel, M. Potel, M. Sergent, M. Decroux and Ø. Fischer, *Mat. Res. Bull.*, 1980, **15**, 867.

43 P. Gougeon, M. Potel and M. Sergent, *Acta Cryst.*, 1989, **C45**, 1285.

44 C. Candolfi, M. Misek, P. Gougeon, R. Al Rahal Al Orabi, P. Gall, R. Gautier, S. Migot, J. Ghanbaja, J. Kastil, P. Levinsky, J. Hejtmanek, A. Dauscher, B. Malaman and B. Lenoir, *Phys. Rev. B*, 2020, **101**, 134521.

45 P. Gougeon, P. Gall, S. Misra, A. Dauscher, C. Candolfi and B. Lenoir, *Mater. Res. Bull.*, 2021, **136**, 111152.

46 V. Petricek, M. Dusek and L. Palatinus, JANA2006 Crystallographic computing system, 2006.

47 E. Alleno, D. Bérardan, C. Byl, C. Candolfi, R. Daou, R. Decourt, E. Guilmeau, S. Hébert, J. Hejtmanek, B. Lenoir, P. Masschelein, V. Ohorodniichuk, M. Pollet, S. Populoh, D. Ravot, O. Rouleau and A. M. Soulier, *Rev. Sci. Instrum.*, 2015, **86**, 011301.

48 R. Chevrel, M. Sergent and J. Prigent, *J. Solid State Chem.*, 1971, **3**, 515–519.

49 O. Peña, *Physica C*, 2015, **514**, 95–112.

50 L.-E. Edshammar in *X-Ray Studies on Binary Alloys of Aluminium with Platinum Metals*, Dissertation, University of Stockholm, 1969.

51 S. Lidin,T. Popp, M. Somer, and H. G. von Schnering, *Angew. Chem. Int. Ed. Engl.* 1992, **31**, 924–927.

52 I. D. Brown and D. Altermatt, *Acta Crystallogr. Sect. B*, 1985, **41**, 244–247.

53 K. Suekuni, M. A. Avila, K. Umeo and T. Takabatake, *Phys. Rev. B*, 2007, **75**, 195210.

54 G. S. Nolas, J. L. Cohn, J. S. Dyck, C. Uher and J. Yang, *Phys. Rev. B*, 2002, **65**, 165201.

55 A. Bentien, E. Nishikori, S. Paschen and B. B. Iversen, *Phys. Rev. B*, 2005, **71**, 144107.

56 D. J. Safarik, T. Klimczuk, A. Llobert, D. D. Byler, J. C. Lashley and J. R. O'Brien, *Phys. Rev. B*, 2012, **85**, 014103.

57 M. M. Koza, H. Mutka, Y. Okamoto, J.-I. Yamaura and Z. Hiroi, *Phys. Chem. Chem. Phys.*, 2015, **15**, 24837.

58 K. Suekuni, K. Tsuruta, M. Kunii, H. Nishiate, E. Nishibori, S. Maki, M. Ohta and A. Yamamoto, M. Koyano, *J. Appl. Phys.*, 2013, **113**, 043712.

59 Y. Bouyrie, C. Candolfi, S. Pailhès, M. M. Koza, B. Malaman, A. Dauscher, J. Tobola, O. Boisron, L. Saviot and B. Lenoir, *Phys. Chem. Chem. Phys.*, 2015, **17**, 19751.

60 M. K. Jana, K. Pal, A. Warankar, P. Mandal, U. V. Waghmare and K. Biswas, *J. Am. Chem. Soc.*, 2017, **139**, 4350.

61 M. Dutta, S. Matteppanavar, M. V. D. Prasad, J. Pandey, A. Warankar, P. Mandal, A. Soni, U. V. Waghmare and K. Biswas, *J. Am. Chem. Soc.*, 2019, **141**, 20293.

62 R. Baumbach, F. Bridges, L. Downward, D. Cao, P. Chesler and B. C. Sales, *Phys. Rev. B*, 2005, **71**, 024202.

63 T. Takabatake, K. Suekuni, T. Nakayama and E. Kaneshita, *Rev. Mod. Phys.*, 2014, **86**, 669.

64 N. Ghassemi, X. Lu, Y. Tian, E. Conant, Y. Yan, X. Zhou and J. H. Ross, *ACS Appl. Mater. Interfaces*, 2018, **10**, 36010.

65 T. Nakayama and E. Kaneshita, *J. Phys. Soc. Jpn.*, 2011, **80**, 104604.

66 Z. Liu, W. Zhang, W. Gao and T. Mori, *Energy Environ. Sci.*, 2021, **14**, 3579–3587.

67 Q. Guo, A. Assoud and H. Kleinke, *Adv. Energy Mater.*, 2014, **4**, 1400348.

68 G. J. Snyder, M. Christensen, E. Nishibori, T. Caillat and B. B. Iversen, *Nat. Mater.*, 2004, **3**, 458–463.

69 S. Misra, C. Barreteau, J. C. Crivello, V. M. Giordano, J. Castellan, Y. Sidis, P. Levinský, J. Hejtmánek, B. Malaman, A. Dauscher, B. Lenoir, C. Candolfi and S. Pailhès, *Phys. Rev. Res.*, 2020, **2**, 043371.

70 S. Misra, P. Levinsky, A. Dauscher, G. Medjahdi, J. Hejtmanek, B. Malaman, G. J. Snyder, B. Lenoir and C. Candolfi, *J. Mater. Chem. C*, 2021, **9**, 5250–5260.

71 S. Misra, A. Léon, P. Levinský, J. Hejtmánek, B. Lenoir and C. Candolfi, *J. Mater. Chem. C*, 2021, **9**, 14490–14496.

72 S. Misra, P. Levinský, J. Hejtmánek, C. Candolfi and B. Lenoir, *ACS Appl. Energy Mater.* DOI: 10.1021/acsaem.2c02364 (2022).

73 P. Gougeon, P. Gall, S. Migot, J. Ghanbaja, M. Hervieu, P. Levinsky, J. Hejtmanek, A. Dauscher, B. Malaman, B. Lenoir and C. Candolfi, *Mater. Adv.*, 2021, **2**, 6020–6030.

74 D. G. Cahill, S. K. Watson and R. O. Pohl, *Phys. Rev. B*, 1992, **46**, 6131–6140.

75 L. Gannon, L. Boeri, C. A. Howard, P. Gougeon, P. Gall, M. Potel, D. Salloum, A. P. Petrovic and M. Hoesch, *Phys. Rev. B*, 2018, **98**, 014104.

76 Z. Liu, N. Sato, W. Gao, K. Yubuta, N. Kawamoto, M. Mitome, K. Kurashima, Y. Owada, K. Nagase, C.-H. Lee, J. Yi, K. Tsuchiya and T. Mori, *Joule*, 2021, **5**, 1196–1208.

Table 1. Relevant Parameters of the Single Crystal Data Collection and Structure Refinement of the Crystal Structure of $Cu_{2.9}K_2Mo_{15}Se_{19}$.

Empirical formula	$Cu_{2.9}K_2Mo_{15}Se_{19}$
Molar mass ($g.mol^{-1}$)	3201.8
Temperature	293 K
Symmetry	Trigonal
Space group	$R\bar{3}c$
a, c (Å)	9.9062 (2), 58.1633 (13)
V (Å^3)	4943.04 (18)
Z	6
ρ ($g\ cm^{-3}$)	6.454
Shape, size (mm^3)	0.159 × 0.140 × 0.083
Radiation	Mo Kα$_1$ (0.71073 Å)
θ range (°)	3.67 – 34.99
Absorption coefficient (mm^{-1})	28.551
Limiting indices	$-15\leq h\leq 15$, $-15\leq k\leq 15$, $-91\leq l\leq 93$
Reflection collected/unique	39633 / 2423
R_{int}	0.0961
Refinement method	Full-matrix least-squares on F^2
Data / parameters	2047 / 82
Final R indices [$I>2\sigma(I)$]	R1=0.0319, wR2=0.1012
R indices (all data)	R1=0.0417, wR2=0.1089
Largest diff. peak and hole ($eÅ^{-3}$)	1.52 and −1.55
Goodness-of-fit on F^2	1.56

Table 2. Site Occupation Factors, Fractional Atomic Coordinates and Equivalent Isotropic Thermal Displacement Parameters for the Crystal Structure of $Cu_{2.9}K_2Mo_{15}Se_{19}$.

Atom	*Wyckoff*	*s.o.f.*	*x*	*y*	*z*	U_{eq} (Å^2)
Mo1	36*f*	1	0.64944(4)	-0.51985(4)	0.352540(6)	0.01472(13)
Mo2	36*f*	1	0.85119(4)	-0.15805(4)	0.288517(7)	0.01551(13)
Mo3	18*e*	1	0.84254(5)	0	0.25	0.01499(15)
Se1	36*f*	1	0.63046(5)	-0.38382(5)	0.315272(8)	0.01961(16)
Se2	36*f*	1	0.65027(5)	-0.31046(5)	0.380542(8)	0.01909(16)
Se3	18*e*	1	0.69698(6)	-0.30302(6)	0.25	0.01909(18)
Se4	12*c*	1	0.6667	-0.6667	0.387302(14)	0.02089(18)
Se5	12*c*	1	1	0	0.324249(14)	0.02093(19)
K	12*c*	1	1	0	0.38771(6)	0.0522(9)
Cu1	36*f*	0.206(4)	0.7319(7)	-0.1796(5)	0.34182(7)	0.043(2)
Cu2	36*f*	0.183(4)	0.6220(7)	-0.2374(6)	0.34333(7)	0.035(2)
Cu3	18*e*	0.188(5)	0.4426(7)	-0.5574(7)	0.25	0.078(4)

Table 3. Details of the data collection and structural refinement of the PXRD pattern of the $Cu_3In_2Mo_{15}Se_{19}$ compound.

Crystal data	
Chemical formula	$Cu_3In_2Mo_{15}Se_{19}$
Molar mass (g mol^{-1})	3359.6
Crystal system, space group	Trigonal, $R\bar{3}c$
Temperature (K)	293
a, *c* (Å)	9.77660 (13), 57.5643 (8)
V (Å^3)	4764.97 (11)
Z	6
Radiation type	Cu Kα_1, λ = 1.54051 Å
Specimen shape, size (μm)	Flat sheet, 25×25×2

Data collection	
Diffractometer	Bruker D8 ADVANCE diffractometer
Specimen mounting	Packed powder pellet
Data collection mode	Reflection
Scan method	Step
2θ values (°)	$2\theta_{min}$ = 8 $2\theta_{max}$ = 120.00 $2\theta_{step}$ = 0.01

Refinement	
R factors and goodness of fit	R_p = 0.093, R_{wp} = 0.124, R_{exp} = 0.049, $R(F)$ = 0.038, χ^2 = 6.452
No. of data points	14256
No. of parameters	61

Table 4. Fractional Atomic Coordinates and Isotropic Thermal Displacement Parameters for the Crystal Structure of $Cu_3In_2Mo_{15}Se_{19}$.

Atom	*Wyckoff*	*x*	*y*	*z*	U_{eq} (Å^2)
Mo1	36*f*	0.83249(19)	0.4820(2)	0.35284(3)	0.0018(4)
Mo2	36*f*	0.48406(19)	0.6565(2)	0.37770(3)	0.0043(5)
Mo3	18*e*	0.3333	0.5052(2)	0.4167	0.0045(7)
Se1	36*f*	0.7039(2)	0.6572(3)	0.35040(4)	0.0046(6)
Se2	36*f*	0.3003(2)	0.3414(2)	0.37982(4)	0.0070(7)
Se3	18*e*	0.6403(3)	0.6667	0.4167	0.0065(9)
Se4	12*c*	0.6667	0.3333	0.38875(6)	0.0088(11)
Se5	12*c*	0.3333	0.6667	0.34262(6)	0.0075(11)
Cu	18*e*	0.3333	0.2226(5)	0.4167	0.192(7)
In	12*c*	0.3333	0.6667	0.04506(5)	0.0372(13)

Table 5. Selected Interatomic Distances (in Å) in $K_2Mo_{15}Se_{19}$ (Ref. 32) and $Cu_{2.9}K_2Mo_{15}Se_{19}$.

	$K_2Mo_{15}Se_{19}$	**$Cu_{2.9}K_2Mo_{15}Se_{19}$**
Mo_6Se_8 unit		
Mo1−Mo1 (x2) intratriangle	2.6799(3)	2.6791(6)
Mo1−Mo1 (x2) intertriangle	2.7675(3)	2.7174(5)
Mo1−Mo2 intercluster	3.459(2)	3.5686(7)
Mo1−Se4	2.5374(4)	2.5456(6)
Mo1−Se2	2.5898(3)	2.6340(7)
Mo1−Se1	2.5968(3)	2.5846(5)
Mo1−Se1	2.5967(4)	2.6083(6)
	2.6030(3)	2.6097(7)
Mo_9Se_{11} unit		
Mo2−Mo2 (x2) intratriangle	2.6682(3)	2.6361(5)
Mo3−Mo3 (x2) intratriangle	2.6821(3)	2.7017(6)
Mo2−Mo3 intertriangle	2.7138(2)	2.6802(4)
		2.7589(5
Mo2−Se5	2.5370(4)	2.5760(6
Mo2−Se2	2.5818(3)	2.6109(8
Mo2−Se2	2.6105(3)	2.6493(9)
Mo2−Se1	2.6563(3)	2.7045(5)
Mo2−Se3	2.7123(3)	2.6872(5)
Mo3−Se2 (x2)	2.5345(3)	2.5698(6)
Mo3−Se3 (x2)	2.5933(3)	2.6003(5)
K−Se1 (x3)	3.7959(8)	3.853(2)
K−Se2 (x3)	3.2255(3)	3.3136(6)
K−Se3 (x3)	3.7891(7)	3.8499(16)
K−Se4	3.4256(15)	3.392(4)
K−Se5	3.6760(15)	3.691(4)
Cu1-Se1		2.499(6)
Cu1-Se2		2.522(4)
Cu1-Se5		2.557(6)
Cu2-Se1		2.213(6)
Cu2-Se1		2.590(6)
Cu2-Se2		2.343(5)
Cu2-Se5		2.523(6)
Cu3-Se2		2.510(5)
Cu3-Se2		2.510(5)
Cu3-Se3		2.520(5)
Cu3-Se4		3.379(7)
Cu3-Se4		3.379(7)

Table 6. Selected Interatomic Distances (in Å) in $In_2Mo_{15}Se_{19}$, $Ag_3In_2Mo_{15}Se_{19}$ and $Cu_3In_2Mo_{15}Se_{19}$.

	$In_2Mo_{15}Se_{19}$	**$Ag_3In_2Mo_{15}Se_{19}$**	**$Cu_3In_2Mo_{15}Se_{19}$**
Mo_6Se_8 unit			
Mo1−Mo1 (x2) intratriangle	2.686(2)	2.6784(3)	2.675(3)
Mo1-Mo1 (x2) intertriangle	2.772(10)	2.7007(2)	2.725(3)
Mo1−Mo2	3.389(3)	3.5694(4)	3.478(4)
Mo1−Se4	2.548(6)	2.5812(4)	2.580(3)
Mo1−Se2	2.589(7)	2.6340(4)	2.600(2)
Mo1−Se1	2.559(7)	2.5726(3)	2.560(3)
Mo1−Se1	2.590(2)	2.5854(3)	2.586(4)
Mo1−Se1	2.605(2)	2.6173(4)	2.620(4)
Mo_9Se_{11} unit			
Mo2−Mo2 (x2) intratriangle	2.674(2)	2.6455(2)	2.643(4)
Mo3−Mo3 (x2) intratriangle	2.680(4)	2.7334(4)	2.734(2)
Mo2−Mo3 intertriangle	2.808(6)	2.7763(2)	2.772(2)
	2.712(5)	2.6820(2)	2.685(2)
Mo2−Se5	2.533(5)	2.5339(4)	2.531(3)
Mo2−Se2	2.582(2)	2.5675(4)	2.573(3)
Mo2−Se2	2.638(2)	2.6538(5)	2.683(2)
Mo2−Se1	2.641(5)	2.6947(3)	2.687(2)
Mo2−Se3	2.715(5)	2.6699(2)	2.659(3)
Mo3−Se2 (x2)	2.542(7)	2.6264(4)	2.600(2)
Mo3−Se3 (x2)	2.600(2)	2.5729(3)	2.579(2)
In−Se5	3.593(6)	2.9893(12)	3.128(4)
In−Se2 (x3)	3.162(2)	3.2806(2)	3.1571(14)
In−Se1 (x3)	3.726(5)	3.5812(6)	3.537(3)
In−Se3 (x3)	3.800(4)	4.199(6)	4.047(2)
In-Se4	3.468(4)	3.895(4)	3.810(4)
Ag/Cu−Se2		2.677(3)	2.514(19)
Ag/Cu−Se2		2.726(3)	2.61(2)
Ag/Cu−Se3		2.5885(9)	2.487(11)
Ag/Cu−Se4		2.881(2)	2.828(14)

Figure Captions

Fig. 1 Crystal structure of the a) $Cu_3In_2Mo_{15}Se_{19}$ and b) $Cu_3K_2Mo_{15}Se_{19}$ compounds projected along the [110] direction, highlighting the different distributions of the Cu^+ cations inserted in the intercluster voids. The ellipsoids representing the Cu^+ cations are orientated along the $[841]$, $[\bar{4}41]$, and $[\bar{4}\bar{8}1]$ directions.

Fig. 2 View of the $Mo_6Se_8Se_6$ and $Mo_9Se_{11}Se_6$ units with their numbering scheme.

Fig. 3 Cu^+ occupation of the distorted triangular bipyramidal and octahedral sites located between adjacent Edshammar polyhedra occupied by the K^+ cations. The Cu^+ and K^+ cations are represented by ellipsoids in light blue and grey, respectively. The Se atoms are shown in red.

Fig. 4 Se polyhedral environments of the Cu^+ cations in $Cu_3K_2Mo_{15}Se_{19}$.

Fig. 5 Se polyhedral environment of the K^+ cations in $Cu_3K_2Mo_{15}Se_{19}$.

Fig. 6 Evolution of the Mo-Mo distances (Å) between $K_2Mo_{15}Se_{19}$ (left values) and $Cu_{2.9}K_2Mo_{15}Se_{19}$ (right values).

Fig. 7 Selected area electron diffraction patterns, HAADF and ABF images for $Cu_3K_2Mo_{15}Se_{19}$ (panels a, b and c) and $Cu_4In_2Mo_{15}Se_{19}$ (panels d, e and f) along the [100] and [001] zone axes, respectively. Fragments of the crystal structure projected along the corresponding zone axis are overlaid on the HAADF and ABF images. The insets in panels b and c are magnifications of

the main image. Panel b shows the zigzag chains formed the two cluster units Mo_9Se_{11} and Mo_6Se_8, highlighting the intercluster voids between two consecutive chains where the K^+ cations reside. In panel c, the K^+ and Cu^+ cations are shown, while the Mo-Se clusters are still visible. Note that, for sake of clarity, the fragment of the crystal structure overlaid in panel c has been drawn by considering full occupancy of Cu^+ cations on their respective sites. In panels b and e, the Se atoms are shown in green, the Mo atoms in red and the In^+ cations in light blue. In panels c and f, the K^+ and Cu^+ cations are in light and dark blue, respectively. In panel f, Cu^+ cations and Se atoms can be observed while the troughs of intensity correspond to Mo and In^+ cations.

Fig. 8 Temperature dependence of the a) electrical resistivity ρ and b) thermopower α for the $Cu_3In_2Mo_{15}Se_{19}$, $Cu_4In_2Mo_{15}Se_{19}$ and $Cu_3K_2Mo_{15}Se_{19}$ compounds. The color-coded symbols are similar in both panels.

Fig. 9 Temperature dependence of the a) total thermal conductivity κ and b) lattice thermal conductivity κ_L for the $Cu_3In_2Mo_{15}Se_{19}$, $Cu_4In_2Mo_{15}Se_{19}$ and $Cu_3K_2Mo_{15}Se_{19}$ compounds. The color-coded symbols are similar in both panels. The horizontal solid line in panel b) stands for the minimum thermal conductivity κ_{min} estimated from the measured sound velocities. The experimental data above ~230 K have been discarded due to the contribution of thermal radiations that accompanies low-temperature measurements of κ.

Fig. 10 Dimensionless thermoelectric figure of merit *ZT* as a function of temperature for the $Cu_3In_2Mo_{15}Se_{19}$, $Cu_4In_2Mo_{15}Se_{19}$ and $Cu_3K_2Mo_{15}Se_{19}$ compounds.

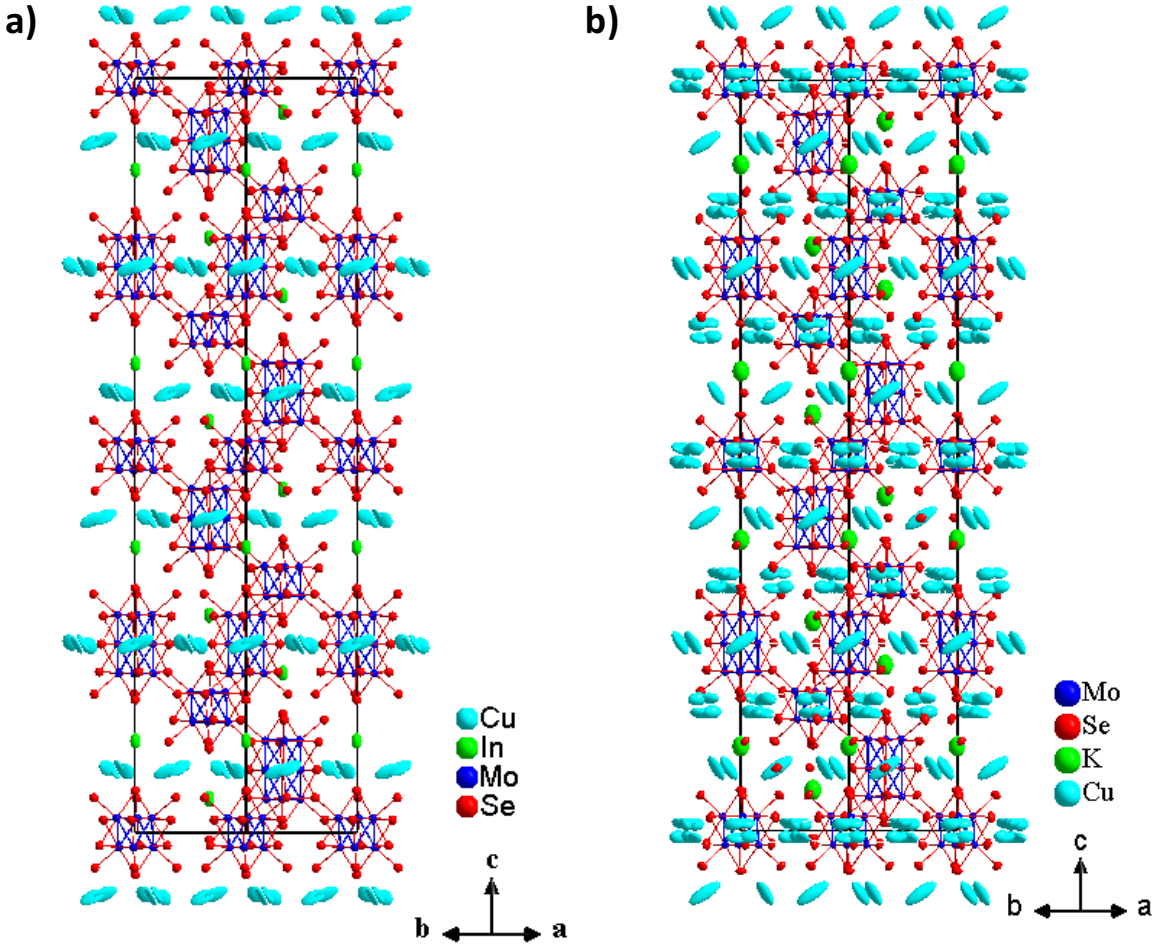

Figure 1

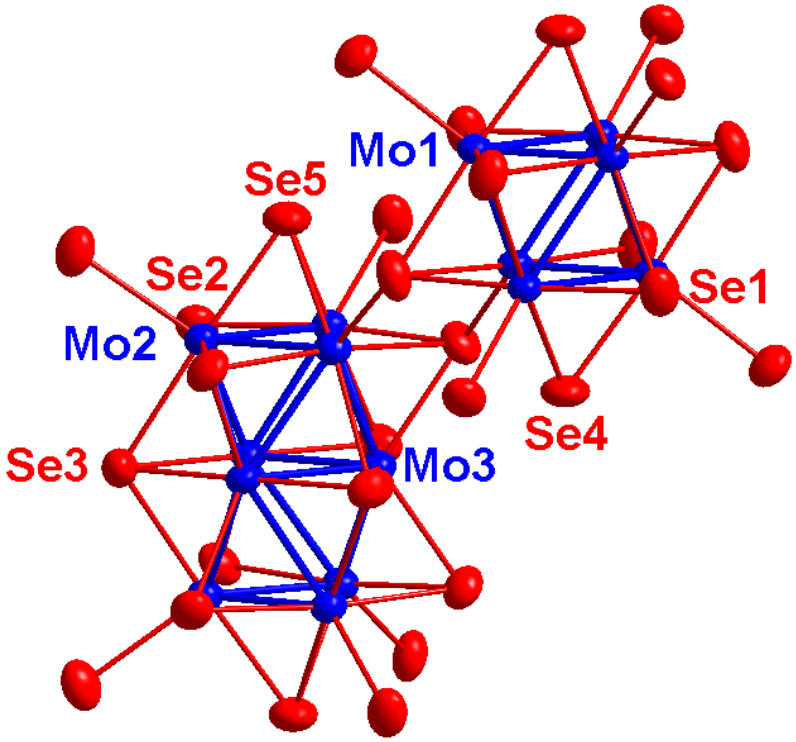

Figure 2

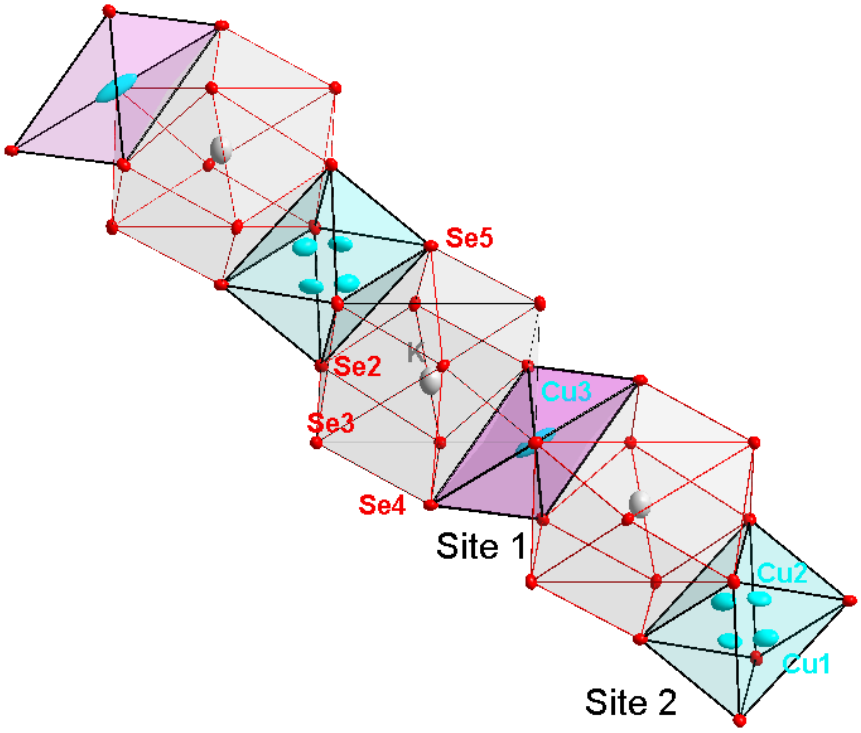

Figure 3

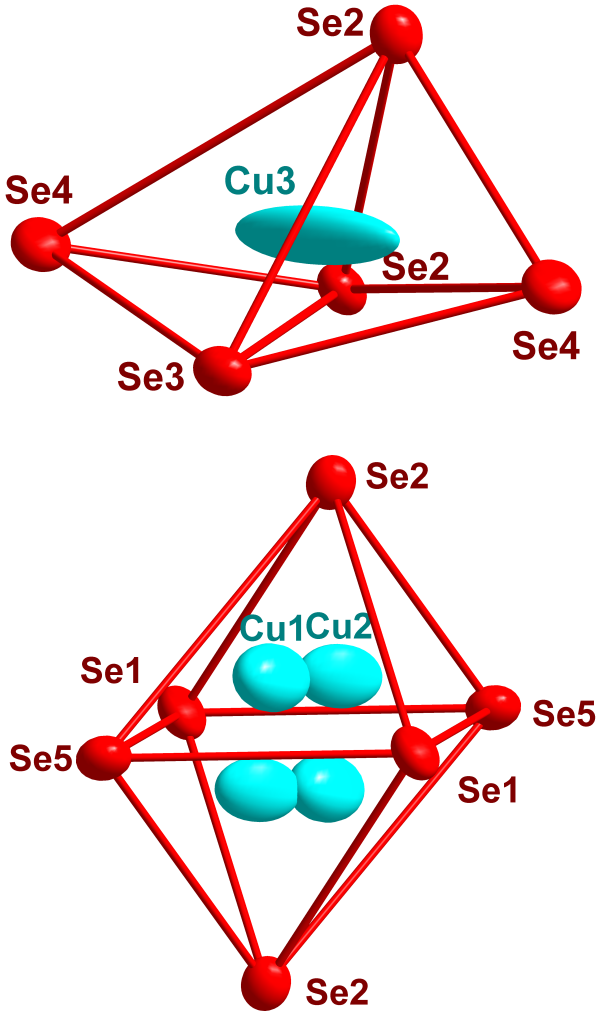

Figure 4

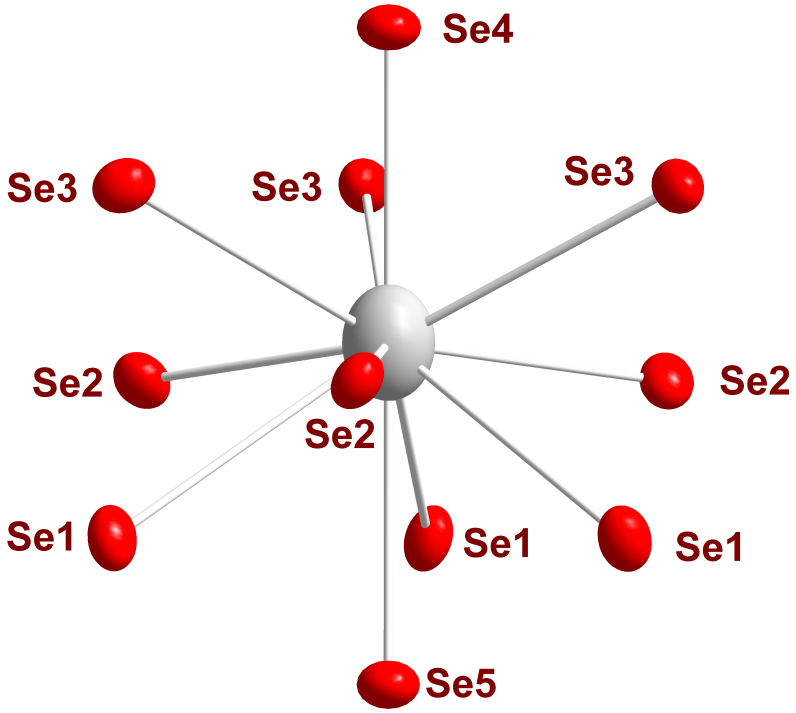

Figure 5

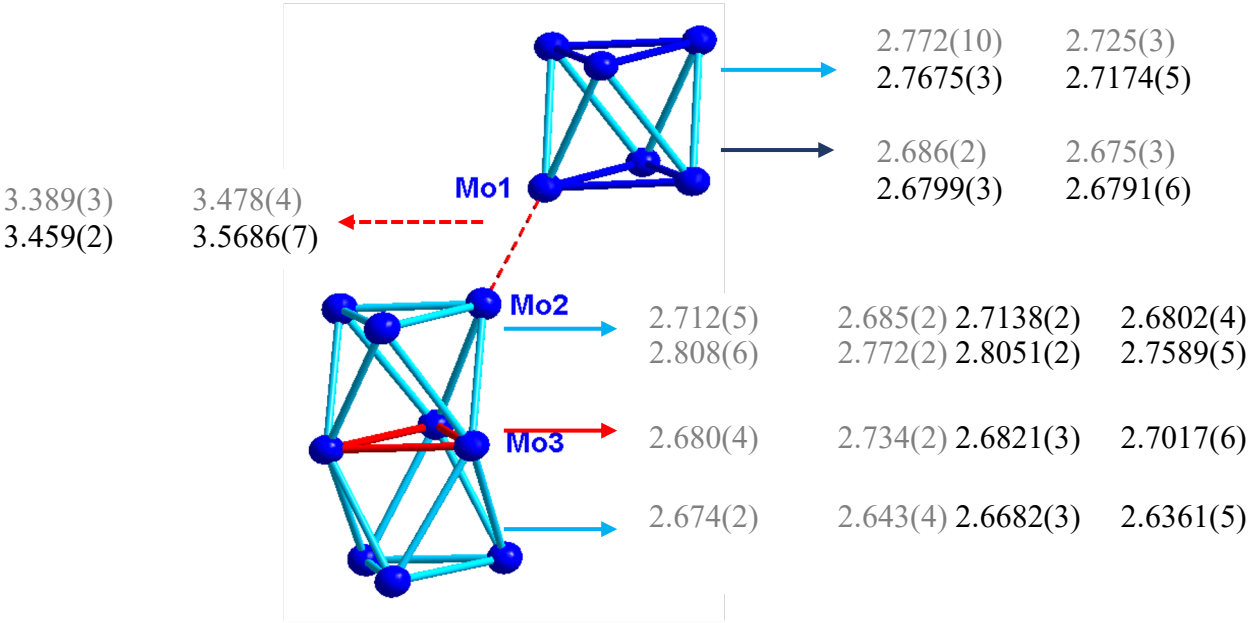
2.772(10) 2.725(3)
2.7675(3) 2.7174(5)
2.686(2) 2.675(3)
2.6799(3) 2.6791(6)
3.389(3) 3.478(4)
3.459(2) 3.5686(7)
Mo1
Mo2
Mo3
2.712(5) 2.685(2) 2.7138(2) 2.6802(4)
2.808(6) 2.772(2) 2.8051(2) 2.7589(5)
2.680(4) 2.734(2) 2.6821(3) 2.7017(6)
2.674(2) 2.643(4) 2.6682(3) 2.6361(5)

Figure 6

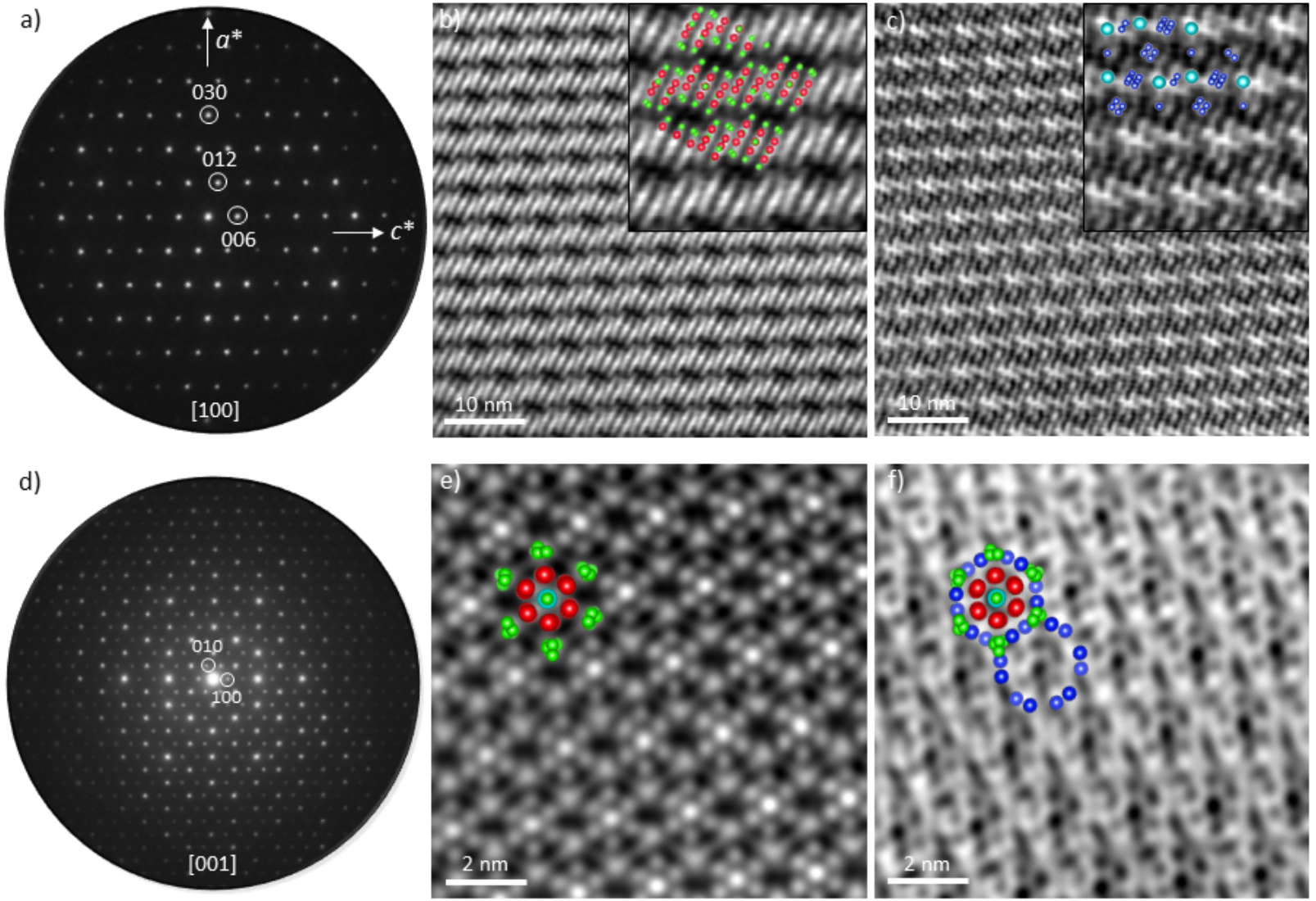

Figure 7

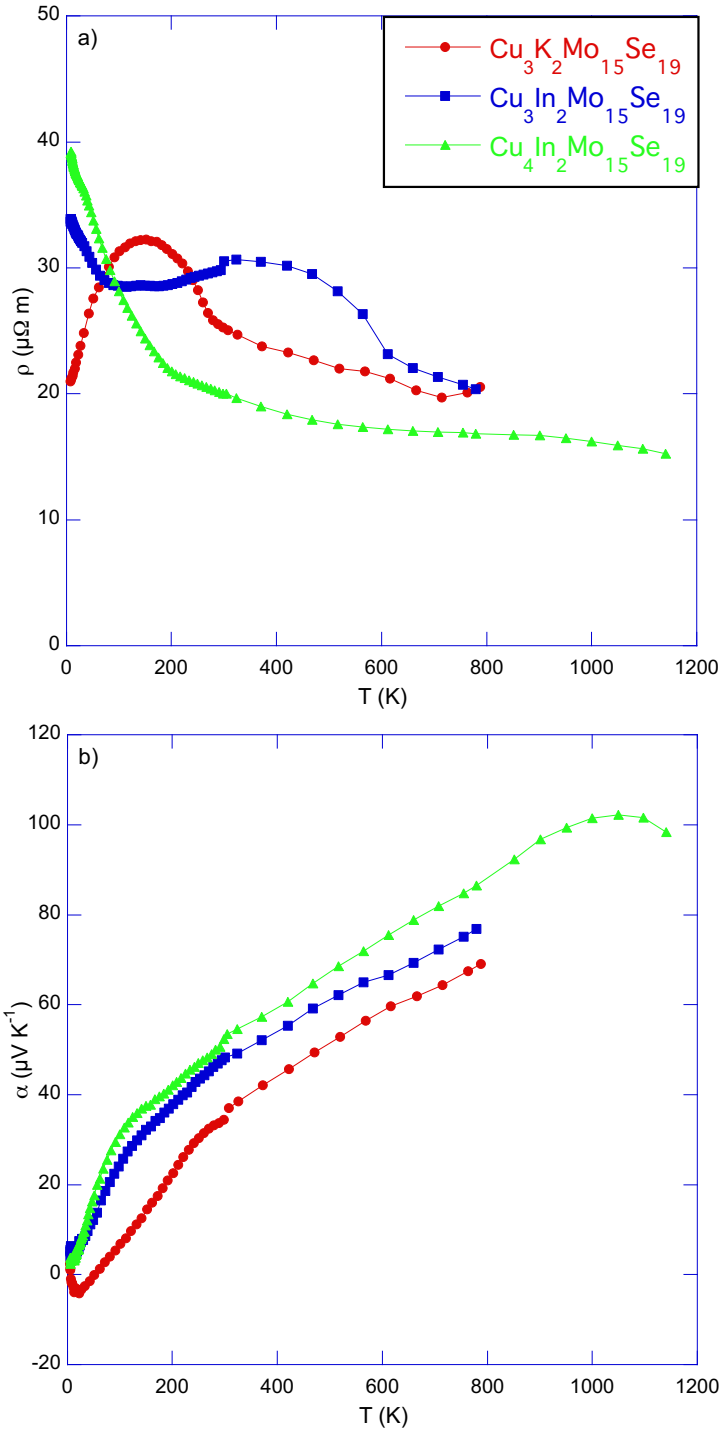
a)
Cu3K2Mo15Se19
Cu3In2Mo15Se19
Cu4In2Mo15Se19
ρ (μΩ m)
T (K)
b)
α (μV K-1)
T (K)

Figure 8

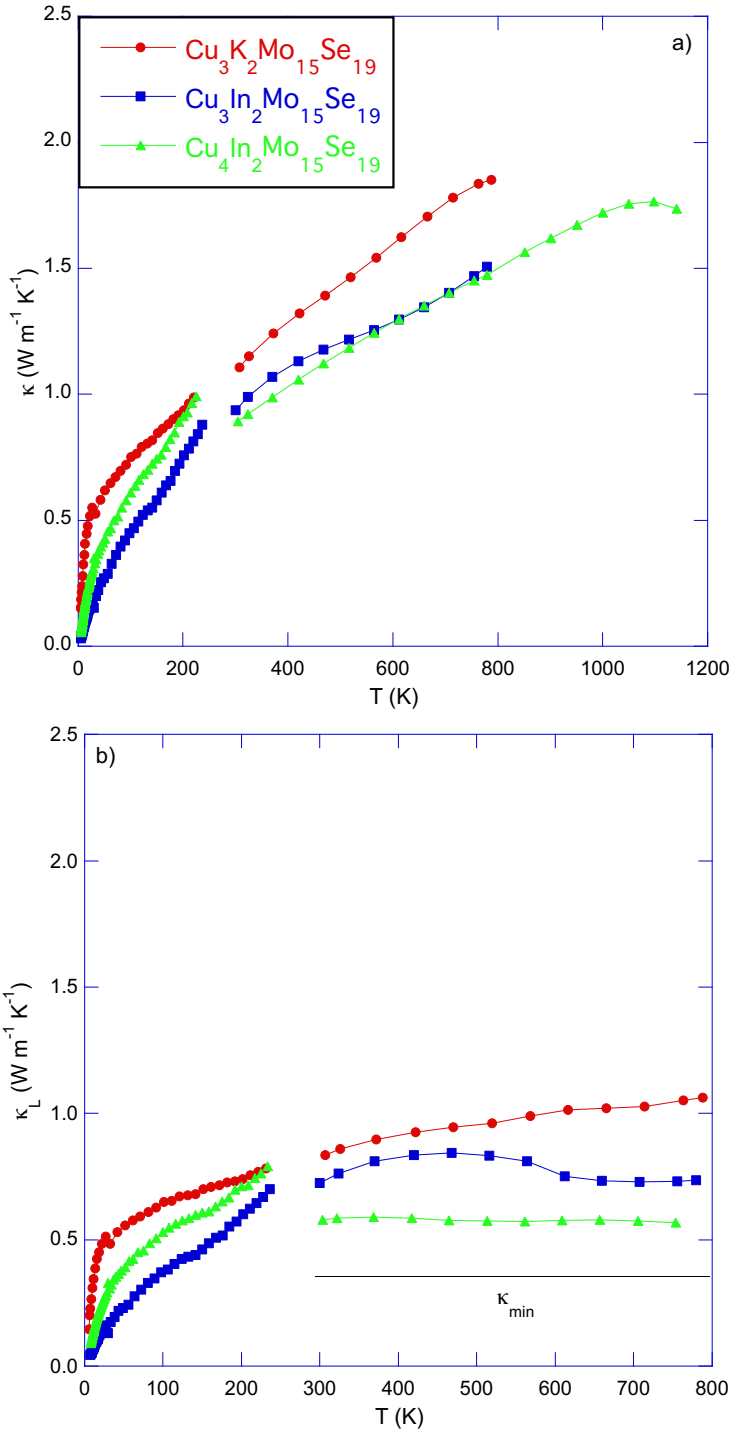
a)
Cu3K2Mo15Se19
Cu3In2Mo15Se19
Cu4In2Mo15Se19
κ (W m-1 K-1)
T (K)
b)
κL (W m-1 K-1)
κmin
T (K)

Figure 9

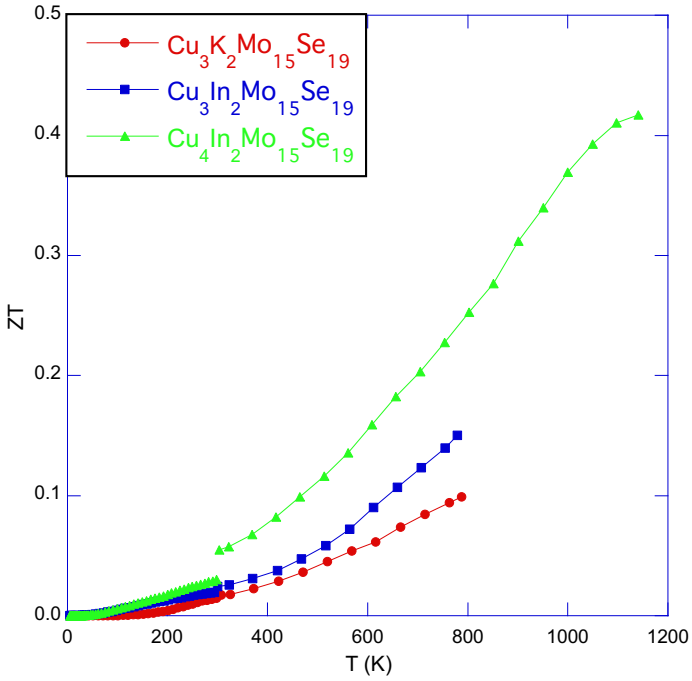
Cu3K2Mo15Se19
Cu3In2Mo15Se19
Cu4In2Mo15Se19
ZT
T (K)
0.0
0.1
0.2
0.3
0.4
0.5
0
200
400
600
800
1000
1200

Figure 10